A WPT System With DC-Link Series/Parallel AC-Link Parallel Rectifiers for AUVs With Multiple Charging Voltages and Currents

Xin Liu, *Member, IEEE*, Ruizhi Chen, Fangli Li, Dehong Zhou, *Senior Member, IEEE*, and Jianxiao Zou, *Member, IEEE*

***Abstract*—Due to the diversity of battery types and capacities, wireless power transfer (WPT) systems for autonomous underwater vehicles (AUVs) have large variations in charging voltages and currents. Conventional solutions of using dc–dc converters to adapt to different specifications may cause increased cost and volume and reduced overall efficiency. To address this issue, this article analyzes the special requirements of the AUV WPT systems. Then, a new AUV WPT system with dc-link series/parallel ac-link parallel rectifiers is proposed for different charging voltages and currents. The generalized mathematical model of the proposed system is presented. The natural current-sharing and voltage-sharing characteristics of the rectifiers are analyzed. In addition, design considerations of the transformers and a detailed design guideline are given. An *LCC*-S WPT prototype with charging voltages of 48 V and 72 V is developed. The output current ranges from 8 A to 36 A and a maximum dc–dc efficiency of 92.1% is obtained under different power transfer distances, which demonstrates the feasibility of the proposed system.**

***Index Terms*—DC-link series/parallel ac-link parallel, different charging voltages and currents, wireless power transfer (WPT).**

I. Introduction

AUTONOMOUS underwater vehicles (AUVs) are a kind of robots that can perform tasks underwater autonomously or remotely without human operation. They are mainly used in underwater exploration, scientific research, monitoring, search and rescue, and military. AUVs are usually powered by battery packs, which mainly have two charging methods: 1) wired charging and 2) wireless power transfer (WPT) [1], [2], [3]. Wired charging uses conductors to deliver current, whereas the WPT technique can transfer power without physical contact [4], [5]. Although the power and overall efficiencies of wired charging may be higher, the WPT technique is more flexible and suitable for underwater applications [6]. It can prevent AUVs from water erosion and mechanical damage, reduce the risk of malfunction due to damaged cables and poor connections, and facilitate automatic charging of AUVs at predetermined locations.

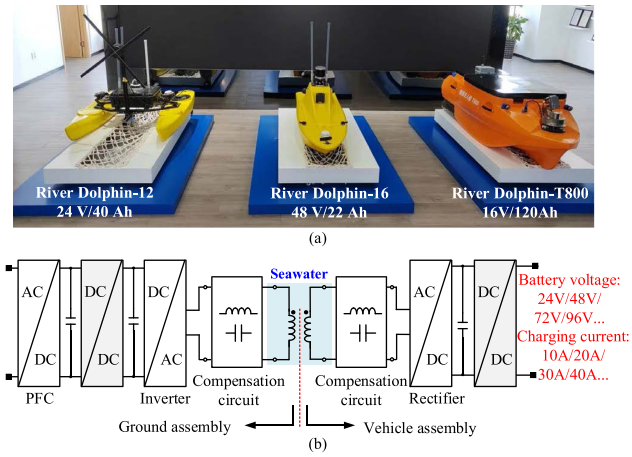

Fig. 1. WPT system for AUVs. (a) Products of AUVs. (b) Schematic of a WPT system for AUVs.

Fig. 1 shows several battery packs and the schematic of the WPT systems for AUVs. As shown in Fig. 1(a), the battery voltages of River Dolphin-T800, River Dolphin-12, and River Dolphin-16 are 16 V, 24 V, and 48 V, respectively. Their battery capacities are 120 Ah, 40 Ah, and 22 Ah, respectively. Different charging voltages and currents are required. Fig. 1(b) presents the schematic of a WPT system for AUVs, which is made up of the ground assembly (GA) and the vehicle assembly (VA). A power factor corrector turns the ac grid voltage into a dc voltage [7]. Alternative dc–dc converters on the GA or VA can be used to obtain desired dc-link voltages. Full-bridge [8] or half-bridge [9] inverters and rectifiers are used for high-frequency dc–ac and ac–dc conversions, respectively. Dual-side compensation circuits can be series-series, series-parallel, parallel-series, parallel-parallel, *LCC–LCC*, and *LCC*-series topologies [10].

Many kinds of research have been proposed for the WPT systems of AUVs, including the magnetic coupler design [11],

Manuscript received 3 February 2024; revised 15 April 2024; accepted 4 May 2024. Date of publication 9 May 2024; date of current version 20 June 2024. This work was supported by the National Natural Science Foundation of China under Grant 52307012. Recommended for publication by Associate Editor K.-B. Park. *(Corresponding author: Jianxiao Zou.)*

Xin Liu and Ruizhi Chen are with the Shenzhen Institute for Advanced Study, University of Electronic Science and Technology of China, Shenzhen 518110, China (e-mail: liu_xin@uestc.edu.cn; 202244060105@std.uestc.edu.cn).

Fangli Li is with the Shenzhen Development and Reform Commission, Shenzhen 518035, China (e-mail: 158277674@qq.com).

Dehong Zhou and Jianxiao Zou are with the School of Automation Engineering, University of Electronic Science and Technology of China, Chengdu 611731, China, and also with the Shenzhen Institute for Advanced Study, University of Electronic Science and Technology of China, Shenzhen 518110, China (e-mail: dhzhou@uestc.edu.cn; jxzou@uestc.edu.cn).

Color versions of one or more figures in this article are available at https://doi.org/10.1109/TPEL.2024.3398990.

Digital Object Identifier 10.1109/TPEL.2024.3398990

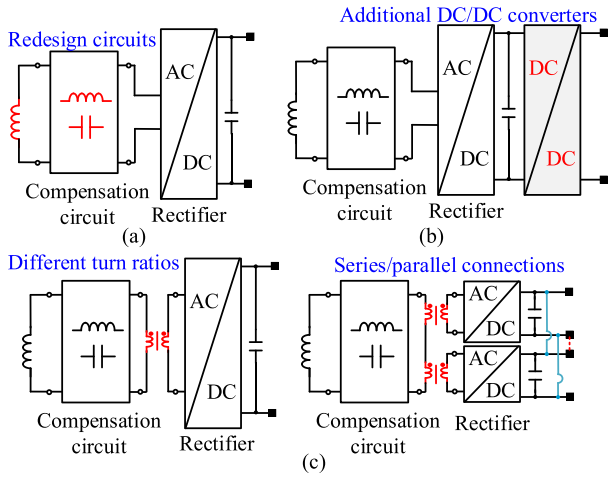

Fig. 2. Methods of adapting to different battery voltages of WPT systems. (a) Redesign VA circuits for each system. (b) Add additional DC–DC converters. (c) Transformer-based solutions.

[12], [13], modulation methods [14], simultaneous wireless power and data transfer [15], system optimization methods [16], positioning tolerance [17], and eddy current loss under seawater [18], [19], [20]. It can be seen from Fig. 1(b) that the output voltages vary a lot. A higher battery voltage can deliver a higher power even with the same current, which can reduce the size and cost of cables significantly. With the increase in battery capacity, a higher battery voltage may appear and the WPT system needs to adapt to different charging voltages. Usually, the battery voltages of the EVs are high which are typically 400 V or 800 V, and the power levels and voltage ranges of different EV models are similar such as the 10 kW/400 V WPT systems for E-HS9 and IM L7 models. However, the WPT systems for AUVs are quite different. The power levels of the WPT systems for various underwater equipment are different and their battery voltages are usually low [16]. Compared with these 400-V and 800-V EV WPT systems, the AUV WPT systems have larger currents and require larger cables, which may reduce the overall efficiency significantly. Conventional WPT designs for EVs may not be suitable for AUVs and related research is urgently needed.

Several methods can be used to adapt to different charging voltages and currents. As shown in Fig. 2(a), the first candidate is to redesign the resonant network [21]. One can change the inductances of the transmitting and receiving coils so that the induced voltage on the VA can be changed. Or, one can change the compensation circuits to obtain a different voltage gain. However, this method requires an entire redesign of the system, which results in difficulties in product development management and maintenance. The second candidate is to apply a BUCK or BOOST converter on the VA side, as shown in Fig. 2(b) [22]. The rectified voltage can be set at a high or low value. Then, the dc–dc converter steps up or down the voltage for different battery packs. This method requires additional hardware circuits, which reduces the efficiency and increases the cost and volume. The third candidate is transformer-based solutions, as shown in Fig. 2(c). In [23], resonant-inductor-integrated-transformer based diode rectifiers are proposed to adapt to 400-V and 800-V WPT systems. One can use transformers with different turn ratios or change the series or parallel connections of two dc-link rectified voltages to adapt to two battery voltages. In [24], the secondary side of the transformers are connected in series or parallel to adapt to 400-V and 800-V WPT systems. However, these two systems are designed for high-voltage EV WPT systems and they are compatible with only two voltages. In addition, additional voltage balancing windings are required in [23] when two rectifiers are connected in series. There are some dc-link series ac-link series and dc-link parallel ac-link series topologies for higher voltage or current. In [25], two active rectifiers are proposed to obtain a wide range of voltage regulation for 48 V applications. Three additional switches are required to change the series or parallel connection of two rectifiers and a voltage unbalance issue exists when using series connection. In addition, such topologies can only apply to one or two application scenarios.

In summary, few works focus on the low-voltage high-current AUV WPT system, especially the compatibility with multiple battery voltages and currents. It occurred to us that a certain AUV only has a fixed battery pack. Although the GA should be the same for various AUVs, different charging voltages can be accommodated by connecting the rectifiers in series and different charging currents can be realized by changing the number of parallel rectifiers. Therefore, this article proposes dc-link series/parallel ac-link parallel (DSPAP) rectifiers for AUV WPT systems with multiple charging voltages and currents. The main contributions of this article are given as follows.

1) A compact *LCC*-S WPT system with DSPAP rectifiers is proposed to obtain a flexible and scalable solution for AUVs with multiple charging voltages and currents.
2) Natural current sharing among parallel rectifiers and natural voltage sharing among series rectifiers are obtained without adding additional components.
3) The mathematical modeling and design principle of the proposed system is presented in detail.
4) An underwater WPT system with multiple low voltages and high currents is experimentally validated.

The rest of this article is organized as follows. Section II presents the proposed system and a mathematical model is established to analyze its power transfer capability. Section III presents the power loss analysis, the natural current and voltage-sharing characteristics, and other design considerations. Section IV demonstrates the experimental results and discussions. Finally, Section V concludes this article.

II. Proposed DSPAP WPT System

In the EV WPT system, the *LCC–LCC* compensation circuits are widely used, which is recommended by SAE J2954 [26]. The *LCC* circuit is still adopted on the GA side due to its high flexibility in parameter design [27]. However, a series compensation circuit with fewer components is used to obtain a more compact VA for the AUV WPT system. This section presents the schematic of the proposed system and establishes its mathematical model for power transfer analysis.

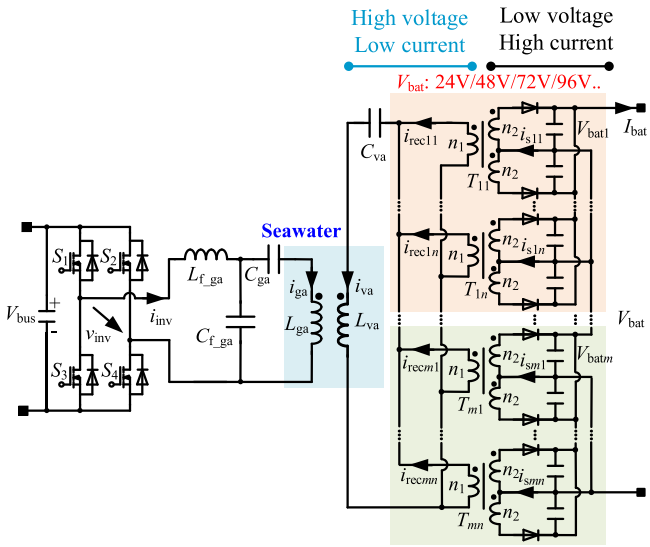

Fig. 3. Proposed low-voltage high-current AUV WPT system with different battery voltages and charging currents.

A. Proposed System

Fig. 3 shows a low-voltage high-current AUV WPT system with different battery voltages and charging currents. To obtain a compact VA, diode rectifiers are used. In addition, the rear-end dc–dc converters are eliminated. $V_{\rm bus}$ and $V_{\rm bat}$ are the dc-link voltages. $I_{\rm bat}$ is the battery charging current. S_1–S_4 represents the metal oxide semiconductor field effect transistors (MOSFETs) of the inverter. $v_{\rm inv}$ and $i_{\rm inv}$ are the inverting voltage and current, respectively. $i_{\rm ga}$ and $i_{\rm va}$ are the resonant currents of the transmitting (Tx) coil and receiving (Rx) coil, respectively. $L_{\rm f\_ga}$ is the filtering inductor on the GA side. $C_{\rm f\_ga}$, $C_{\rm ga}$, and $C_{\rm va}$ are the compensation capacitors. $L_{\rm ga}$ and $L_{\rm va}$ are the inductances of the coupling coils. The coupling coefficient k and mutual inductance M between Tx and Rx coils are defined as

$$M = k\sqrt{L_{\rm ga}L_{\rm va}}. \tag{1}$$

The ac sides of the transformers are connected in parallel, which benefits modular design. The number of the transformers connected in parallel on the dc side is n. There are m groups of these transformers, which are connected in series to adapt to different battery voltages. $V_{\rm bat1}$-$V_{{\rm bat}\,m}$ represent the dc voltages of different groups. T_{11}-T_{mn} represent the transformers that turn the ac-side high voltage and low current into low voltage and high current. $i_{{\rm rec}\,ij}$ and $i_{{\rm s}\,ij}$ are the primary and secondary currents of T_{ij} transformer.

To reduce one forward voltage loss of the diodes, transformers with two secondary windings are used. To ensure current sharing and simplify the manufacturing techniques, the turn ratios of all transformers are the same. n_1 and n_2 are the turns of the primary and secondary sides of the transformers. Since there are two identical secondary windings, the turns ratio should be n_1:n_2:n_2, which is denoted as $N_{\rm va}$ as follows:

$$N_{\rm va} = n_1 : n_2 : n_2. \tag{2}$$

Each AUV will only use one type of these batteries, and the voltage range of each AUV battery is within a certain range. Therefore, the connection between the rectifier and the output can be determined when installing the WPT system. Owing to the modular design of the rectifiers, one can configure different n to obtain different charging currents. A larger n corresponds to a larger $I_{\rm bat}$. In addition, one can configure different m to obtain different charging voltages. A larger m corresponds to a larger $V_{\rm bat}$. Therefore, this topology can adapt to different battery voltages and charging currents of the AUV WPT systems without changing the turns ratios of the transformers.

B. Power Transfer Analysis

Due to the strong filtering effects of the *LCC*-S compensation circuit, the power transfer capacity of the system is almost determined by the fundamental voltages. Thus, the fundamental harmonic approximation (FHA) method is used [23]. In this article, italic letters represent the root mean square (rms) value of a variable.

Fig. 4 shows the equivalent circuits of the proposed DSPAP WPT system. $R_{\rm f\_ga}$, $R_{\rm ga}$, and $R_{\rm va}$ are the parasitic resistances of $L_{\rm f\_ga}$, $L_{\rm ga}$, and $L_{\rm va}$, respectively. Different from the EV WPT system transferring power via the air, the media for AUV WPT systems is seawater. The high-frequency magnetic field can cause a significant eddy current loss in the seawater. The equivalent resistances representing the eddy current losses are determined by the operating frequency and are almost irrelated to the coil currents according to [18] and [28], which are denoted as $R_{\rm eddy1}$ and $R_{\rm eddy2}$. The parasitic resistances of the GA and VA coils in air medium are denoted as $R_{\rm coil1}$ and $R_{\rm coil2}$. For simplicity, these parasitic resistances can be considered constant and as part of $R_{\rm ga}$ and $R_{\rm va}$

$$R_{\rm ga} = R_{\rm eddy1} + R_{\rm coil1} \tag{3}$$

$$R_{\rm va} = R_{\rm eddy2} + R_{\rm coil2}. \tag{4}$$

$R_{\rm s1}$ and $R_{\rm s2}$ are the parasitic resistances of the transformers. $L_{\rm f\_va11}$-$L_{{\rm f\_va}\,mn}$ are the leakage inductances of the transformers. $R_{\rm L11}$-$R_{{\rm L}\,mn}$ are the equivalent resistances of different diode rectifiers. $R_{\rm rec11}$-$R_{{\rm rec}\,mn}$ are equivalent resistances seen from the primary sides of the transformers. $L_{\rm eq}$ and $R_{\rm eq}$ are the total leakage inductance and loading resistance, respectively.

To reduce the reactive power, the system operates at the resonance frequency. According to [23], the resonant conditions of the GA can be expressed as follows:

$$\omega L_{\rm f\_ga} = \frac{1}{\omega C_{\rm f\_ga}} \tag{5}$$

$$\omega L_{\rm ga} = \frac{1}{\omega C_{\rm f\_ga}} + \frac{1}{\omega C_{\rm ga}}. \tag{6}$$

When deriving the resonant currents, the parasitic resistances can be neglected for simplicity. Then, one can obtain the transmitting current as

$$I_{\rm ga} = \frac{V_{\rm inv}}{\omega L_{\rm f\_ga}}. \tag{7}$$

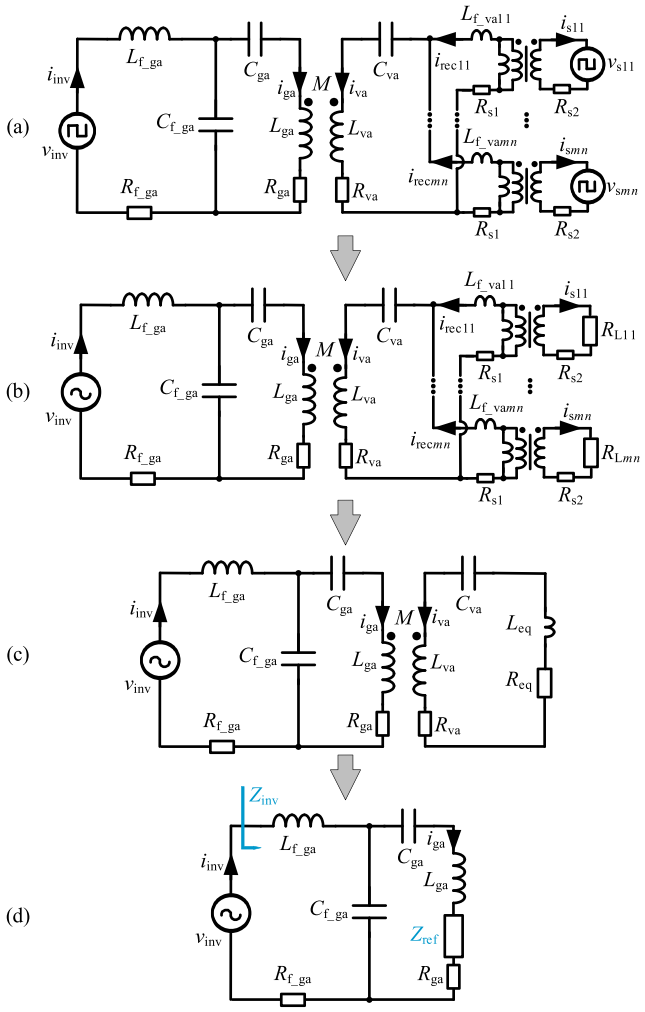

Fig. 4. Equivalent circuits of the proposed system. (a) Equivalent circuit of the system. (b) Equivalent circuit using FHA. (c) Equivalent circuit with a simplified rectifier. (d) Equivalent circuit with a reflected impedance.

On the VA side, L_{va} and L_{eq} resonate with C_{va}

$$\omega(L_{va}+L_{eq})=\frac{1}{\omega C_{va}}. \tag{8}$$

Since all the rectified dc voltages are connected in series, V_{bat} is the sum of $V_{bat\,i}$. In addition, natural voltage sharing can be obtained by the proposed system, which will be discussed in detail in Section III-B

$$V_{bat}=\sum_{i=1}^{m}V_{bat\,i}=mV_{bat1}. \tag{9}$$

According to FHA, one can obtain V_{inv} and $V_{s\,ij}$

$$V_{inv}=\frac{2\sqrt{2}V_{bus}}{\pi} \tag{10}$$

$$V_{s\,ij}=\frac{2\sqrt{2}V_{bat1}}{\pi}. \tag{11}$$

Define P_o as the output power and one can I_{bat} as

$$I_{bat}=\frac{P_o}{V_{bat}}. \tag{12}$$

$I_{bat\,i1}$-$I_{bat\,in}$ represent the rectified currents of #i group diode rectifiers. Natural current sharing can be obtained among different transformers in this system, which will be discussed in Section III-B as well. Based on the law of conservation of energy and neglecting the power loss in the diodes, one can obtain the relationship between $I_{s\,ij}$ and I_{bat}

$$I_{s\,ij}=\frac{\pi I_{bat\,ij}}{2\sqrt{2}}=\frac{\pi I_{bat\,i}}{2\sqrt{2}n}=\frac{\pi I_{bat}}{2\sqrt{2}n}. \tag{13}$$

Thus, one can obtain $I_{rec\,ij}$ as

$$I_{rec\,ij}=\frac{I_{s\,ij}}{N_{va}}=\frac{\pi I_{bat}}{2\sqrt{2}N_{va}n}. \tag{14}$$

Since all the primary sides of the transformers are connected in parallel, I_{va} is the sum of $I_{rec\,i}$

$$I_{va}=\sum_{j=1}^{m}\sum_{i=1}^{n}I_{rec\,ij}\approx\frac{\pi mI_{bat}}{2\sqrt{2}N_{va}}. \tag{15}$$

Theoretically, the power transferred through the coupling coils is approximately equal to P_o, i.e., one can obtain

$$P_o\approx\omega MI_{ga}I_{va}. \tag{16}$$

By combining (9), (15), and (16), the expression of I_{ga} is derived

$$I_{ga}=\frac{P_o}{\omega MI_{va}}=\frac{2\sqrt{2}N_{va}P_o}{\pi m\omega MI_{bat}}=\frac{2\sqrt{2}N_{va}V_{bat1}}{\pi\omega M}. \tag{17}$$

$R_{L\,ij}$ is the equivalent resistance of #ij diode rectifier, which can be expressed as

$$R_{L\,ij}=\frac{8}{\pi^2}R_{bat\,ij}=\frac{8}{\pi^2}\frac{V_{bat\,i}}{I_{bat\,ij}}=\frac{8}{\pi^2}\frac{nV_{bat}}{mI_{bat}}=\frac{8nP_o}{\pi^2mI_{bat}^2}. \tag{18}$$

Considering the loading resistance transformation of the transformers and the parallel connections of all branches in Fig. 4(b), one can obtain the equivalent resistance R_{eq} and inductance L_{eq} in Fig. 4(c) as follows:

$$R_{eq}=\frac{N_{va}^2R_{L\,ij}}{mn} \tag{19}$$

$$L_{eq}=\frac{L_{f\_va\,ij}}{mn}. \tag{20}$$

The reflected impedance Z_{ref} on the GA side in Fig. 4(d) is obtained when neglecting the parasitic resistances

$$Z_{ref}=\frac{\omega^2M^2}{R_{eq}}. \tag{21}$$

Then, the impedance of the inverter is derived

$$Z_{inv}=\frac{1}{\omega^2C_{f\_ga}^2Z_{ref}}=\frac{8P_oN_{va}^2}{\pi^2m^2\omega^4C_{f\_ga}^2M^2I_{bat}^2}. \tag{22}$$

Finally, one can calculate I_{inv} according to

$$I_{inv}=\frac{V_{inv}}{Z_{inv}}=\frac{\omega L_{f\_ga}I_{ga}}{Z_{inv}}=\frac{\pi\sqrt{2}mMC_{f\_ga}\omega^2I_{bat}}{4N_{va}}. \tag{23}$$

According to the above derivations, all the resonant currents can be expressed as the functions of the battery charging voltage and current. Fig. 5 shows the three-dimensional (3-D) plots of

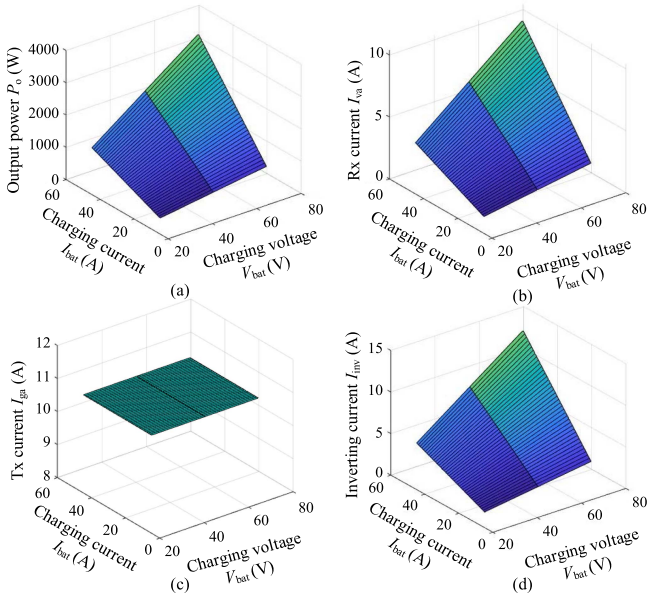

Fig. 5. P_o, I_{va}, I_{ga}, and I_{inv} with respect to V_{bat} and I_{bat}, where $f = 85$ kHz, $k = 0.4$, $N_{va} = 32{:}2{:}2$, $L_{f\_ga} = 45$ μH, $L_{ga} = 153$ μH, $L_{va} = 149$ μH, $C_{f\_ga} = 78$ nF, $C_{ga} = 32$ nF, $C_{va} = 23$ nF. (a) P_o. (b) I_{va}. (c) I_{ga}. (d) I_{inv}.

P_o, I_{va}, I_{ga}, and I_{inv} with respect to V_{bat} and I_{bat}. I_{bat} changes from 5 A to 50 A and V_{bat} are discrete values which are 24 V, 48 V, and 72 V. As can be seen from Fig. 5(a), (b), and (d), P_o, I_{va}, and I_{inv} are proportional to V_{bat} and I_{bat}. Larger V_{bat} and I_{bat} correspond to larger output power, larger Rx current, and inverting current. However, I_{ga} remains unchanged when V_{bat} and I_{bat} vary.

In practical applications, the positions between the Tx and Rx coils may change due to different parking positions. This may cause variations in the coupling coefficient and mutual inductance. According to (13)–(15), I_{va}, $I_{rec\,ij}$, and $I_{s\,ij}$ are irrelated to the mutual inductance and are determined by I_{bat}. However, I_{ga} is inversely proportional to M according to (17), and I_{inv} is proportional to M according to (23). One can regulate the dc-link voltage to obtain the desired I_{ga} against the mutual inductance variation.

III. Design Considerations Of Proposed System

Section II develops the mathematical model of the proposed system and reveals its basic power transfer characteristics. In practical applications, more design considerations should be taken into account, including heat dissipation, overall efficiency estimation, and parameter selection. This section presents a detailed analysis of the power losses, the voltage-sharing and current-sharing characteristics, the transformer design, and the design procedure of the system.

A. Power Loss Analysis

Once the main circuit is determined, one can calculate the power loss and evaluate the overall efficiency, which is demonstrated in this section.

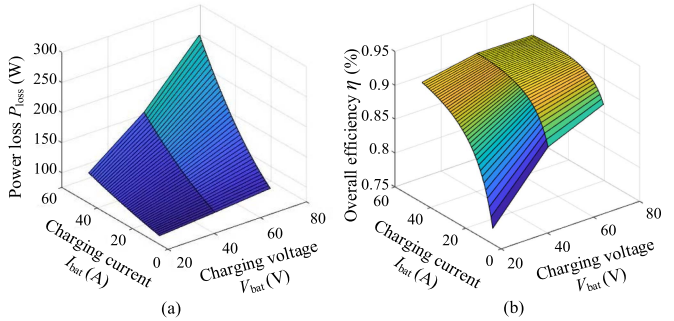

Fig. 6. P_{loss} and η with respect to V_{bat}, and I_{ba}, where $f = 85$ kHz, $k = 0.4$, $N_{va} = 32{:}2{:}2$, $L_{f\_ga} = 45$ μH, $L_{ga} = 153$ μH, $L_{va} = 149$ μH, $C_{f\_ga} = 78$ nF, $C_{ga} = 32$ nF, $C_{va} = 23$ nF, $R_{dson} = 0.01$ Ω, $R_{f\_ga} = 0.04$ Ω, $R_{ga} = 0.5$ Ω, $R_{va} = 0.5$ Ω, $R_{s1} = 1.1$ Ω, $R_{s2} = 8$ mΩ. (a) P_{loss}. (b) η.

The output current of the rectifier in Fig. 3 flows through one diode whose forward voltage is V_f. Therefore, the total power loss in the didoes denoted as P_{dio} is obtained

$$P_{dio} = \sum_{i=1}^{m} V_f I_{bat\,i} = m V_f I_{bat} = \frac{m V_f P_o}{V_{bat}}. \tag{24}$$

$P_{Fe\,ij}$ represents the magnetic core loss of T_{ij} transformer. Since both $V_{bat\,i}$ and the operating frequency remain unchanged with respect to different P_o, the total magnetic core loss P_{Fe} is a constant value

$$P_{Fe} = \sum_{j=1}^{m}\sum_{i=1}^{n} P_{Fe\,ij} = mn P_{Fe11}. \tag{25}$$

Since ZVS operation is achieved, only the conduction losses of the MOSFETs are considered. R_{dson} is the conduction resistance of the MOSFET. Thus, the total power loss of the system P_{loss} can be approximately expressed as

$$P_{loss} = I_{inv}^2 (R_{f\_ga} + 2R_{dson}) + I_{ga}^2 R_{ga} + I_{va}^2 R_{va} + \sum_{j=1}^{m}\sum_{i=1}^{n} (I_{rec\,ij}^2 R_{s1} + I_{s\,ij}^2 R_{s2}) + P_{Fe} + P_{dio}. \tag{26}$$

Once P_o and I_{bat} are determined, one can obtain I_{inv}, I_{ga}, I_{va}, $I_{rec\,ij}$, and $I_{s\,ij}$. Thus, the power loss P_{loss} and then the overall efficiency η can be calculated

$$\eta = \frac{P_o}{P_o + P_{loss}}. \tag{27}$$

Fig. 6 shows the 3-D plots of P_{loss} and η with respect to V_{bat}, I_{bat}, and k. V_{bat} can be 24 V, 48 V, or 72 V, which is determined by the battery packs of the AUVs. A longer range of AUVs usually corresponds to a higher battery voltage. In Fig. 6(a) and (b), the coupling coefficient k remains unchanged. In Fig. 6(a), larger V_{bat} and I_{bat} result in a larger power loss P_{loss} due to the increase of resonant currents. As for the efficiency in Fig. 6(b), it may increase with the increases of V_{bat} and I_{bat} at first, and then it may decrease. The reason is that a larger V_{bat} corresponds to a larger n. According to (13), both the increases of V_{bat} and I_{bat} can result in a larger I_{va}. The parasitic resistance

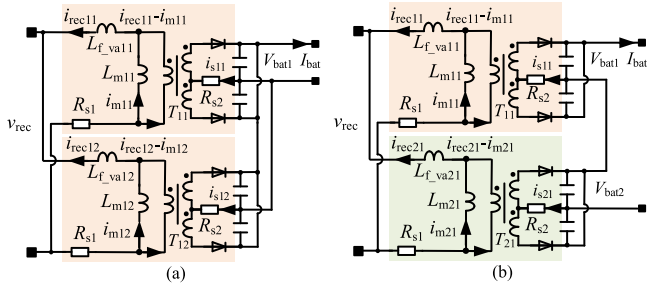

Fig. 7. Equivalent circuits of parallel and series transformers. (a) Parallel rectifiers with a current-sharing characteristic. (b) Series rectifiers with a voltage-sharing characteristic.

of the Rx coil is large, which can cause a significant drop of η when using a large I_{va}.

B. Voltage-Sharing and Current-Sharing Characteristics

Current sharing in parallel converters and voltage sharing in series converters are of great importance for safety operations. This section demonstrates the natural voltage-sharing and current-sharing characteristics of the proposed DSPAP architecture in detail.

For simplicity without loss of generality, two neighborhood rectifiers are analyzed here. Fig. 7(a) and (b) shows the equivalent circuits of two parallel rectifiers and two series rectifiers, respectively. $L_{\mathrm{m}ij}$ and $i_{\mathrm{m}ij}$ are the magnetizing inductance and the magnetizing current of T_{ij} transformer. Since similar transformers are used, the differences among i_{m11}, i_{m12}, and i_{m21} are small and can be neglected. One can obtain the input currents of two transformers

$$i_{\mathrm{rec11}} \approx \frac{v_{\mathrm{rec}} - N_{\mathrm{va}} v_{\mathrm{s11}}}{j\omega L_{\mathrm{f\_va11}}} \tag{28}$$

$$i_{\mathrm{rec12}} \approx \frac{v_{\mathrm{rec}} - N_{\mathrm{va}} v_{\mathrm{s12}}}{j\omega L_{\mathrm{f\_va12}}}. \tag{29}$$

For the parallel rectifiers, the output voltages are the same, which means $v_{\mathrm{s11}} \approx v_{\mathrm{s12}}$. Thus, the currents flowing through the rectifiers are determined by the leakage inductances. It is known that the leakage inductances are related to the turns, the magnetic cores, and the structure of the transformers. Since the same transformers are used, the parameter discrepancies are small, which means i_{rec11} is approximately equal to i_{rec12}. Similar analysis can be extended to other rectifiers and (14) can be obtained. Therefore, the parallel rectifiers have a natural current-sharing characteristic.

According to (14), i_{rec11} is approximately equal to i_{rec21}. All the leakage inductances are similar and its voltage drop is small. One can derive the following equations from Fig. 7(b). Although there may exist a small voltage difference caused by two different transformers $v_{\mathrm{s11}} \approx v_{\mathrm{s21}}$

$$v_{\mathrm{s11}} \approx \frac{v_{\mathrm{rec}} - j\omega L_{\mathrm{f\_va11}} i_{\mathrm{rec11}}}{N_{\mathrm{va}}} \approx \frac{v_{\mathrm{rec}}}{N_{\mathrm{va}}} \tag{30}$$

$$v_{\mathrm{s21}} \approx \frac{v_{\mathrm{rec}} - j\omega L_{\mathrm{f\_va21}} i_{\mathrm{rec21}}}{N_{\mathrm{va}}} \approx \frac{v_{\mathrm{rec}}}{N_{\mathrm{va}}}. \tag{31}$$

According to (11), the relationship between $V_{\mathrm{s}ij}$ and $V_{\mathrm{bat}i}$ is fixed. Thus, the diode rectified voltages are the same. Natural voltage sharing can be achieved

$$V_{\mathrm{bat1}} = V_{\mathrm{bat2}} = \ldots = V_{\mathrm{bat}m} = \frac{V_{\mathrm{bat}}}{m}. \tag{32}$$

C. Design Considerations of Transformers

According to Fig. 7, one can obtain the following equation:

$$i_{\mathrm{rec11}} = \frac{i_{\mathrm{s11}}}{N_{\mathrm{va}}} + i_{\mathrm{m11}}. \tag{33}$$

The diode rectifier can be regarded as a resistive load. Thus, there exists a 90° between i_{m11} and i_{s11}. One can obtain

$$I_{\mathrm{rec11}} = \sqrt{\left(\frac{\pi I_{\mathrm{bat}}}{2\sqrt{2} n N_{\mathrm{va}}}\right)^2 + (I_{\mathrm{m11}})^2}. \tag{34}$$

Since the magnetizing inductance and the applied voltage are given, one can calculate I_{m11} as (35), which is determined by N_{va}, V_{bat1}, ω, and $L_{\mathrm{m}ij}$

$$I_{\mathrm{m11}} = \frac{N_{\mathrm{va}} V_{\mathrm{s11}}}{\omega L_{\mathrm{m11}}} = \frac{2\sqrt{2} N_{\mathrm{va}} V_{\mathrm{bat1}}}{\pi \omega L_{\mathrm{m11}}}. \tag{35}$$

Multiple transformers are connected in parallel and all the magnetizing current flow through the receiving coil. When R_{va} is large, these magnetizing currents may cause serious power losses. According to (34) and current sharing characteristic, one can obtain these power losses, which is denoted as P_{m} in (36). These power losses remain the same even when the output power is zero, which may result in a low overall efficiency at light loading

$$P_{\mathrm{m}} = (mnI_{\mathrm{m11}})^2 R_{\mathrm{va}}. \tag{36}$$

One should pay attention to the magnetizing inductances when designing the transformers. On one hand, a larger magnetizing inductance corresponds to a smaller I_{m11}, which can decrease P_{m}. On the other hand, the system has little requirement on L_{m11} and $L_{\mathrm{f\_va11}}$ and a high coupling coefficient is desired to maximize the power transfer efficiency. Thus, transformers without air gaps are used. The transformers widely used in *LLC* converters utilize a sandwich structure, as shown in Fig. 8, which is also adopted here. The windings are divided into multiple groups, which are connected in parallel to share the large currents. This technique can balance the magnetic potential distribution to reduce the power losses.

Fig. 9 shows the plot of P_{m} with respect to V_{bat1} and L_{m11}. It can be seen that a small L_{m11} can result in a serious increase of P_{m}. In this article, transformers without air gaps are used and L_{m11} increases from conventional several hundreds of μH to 1.6 mH. The corresponding magnetizing current is around 0.4 Arms when V_{bat1} is 24 V and $N_{\mathrm{va}} = 16$. P_{m} is significantly reduced from several hundred watts to a few watts.

D. Design Procedure of Proposed System

To make the proposed system more intuitive, a detailed design procedure with five steps is presented in Fig. 10.

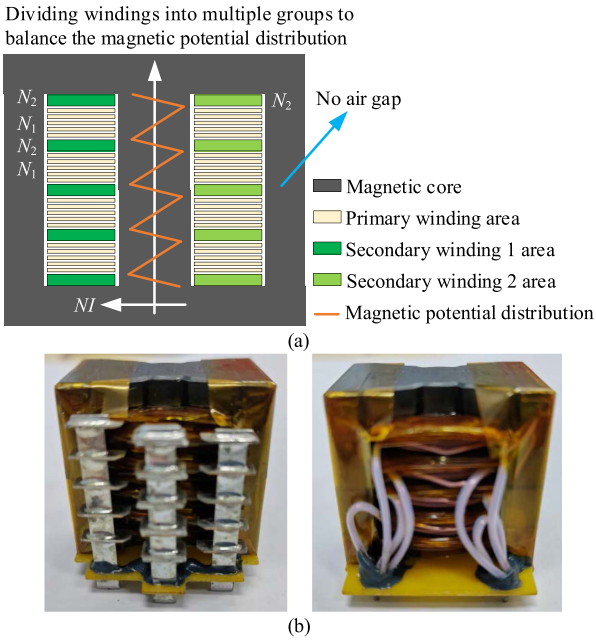

Fig. 8. Design of transformers. (a) Schematic of the transformer. (b) Prototype of the transformer (32:2:2).

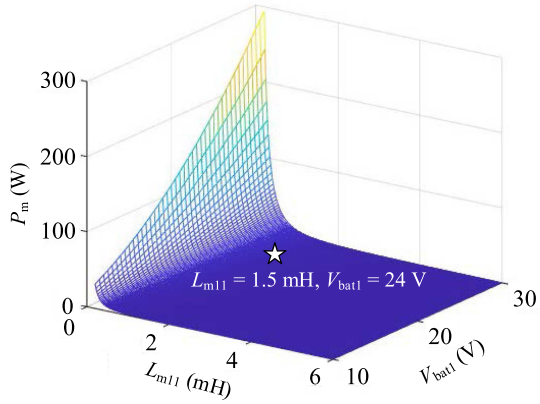

Fig. 9. P_m with respect to V_{bat1} and L_{m11}, where $f = 85$ kHz, $N_{va} = 16$, $m = 2$, $n = 3$, and $R_{va} = 0.5\ \Omega$.

There are different specifications for various AUVs. The first step is to determine the charging voltage and current of the battery pack according to the specific application requirements.

The second step is to choose the numbers of the parallel and series rectifiers, i.e., determining the values of m and n. Afterward, one can design suitable transformers and calculate the resonant currents of different components on the VA based on (12)–(15).

The third step is to design proper coupling coils according to the given dimensions and power transfer distances. An electromagnetic field simulation can be conducted to select the appropriate conductor cross-sectional area and the number of turns. One can also obtain the self-inductances and coupling coefficient of the coils.

The fourth step is to design the *LCC*-S resonant inductors and capacitors according to the coil self-inductances based on

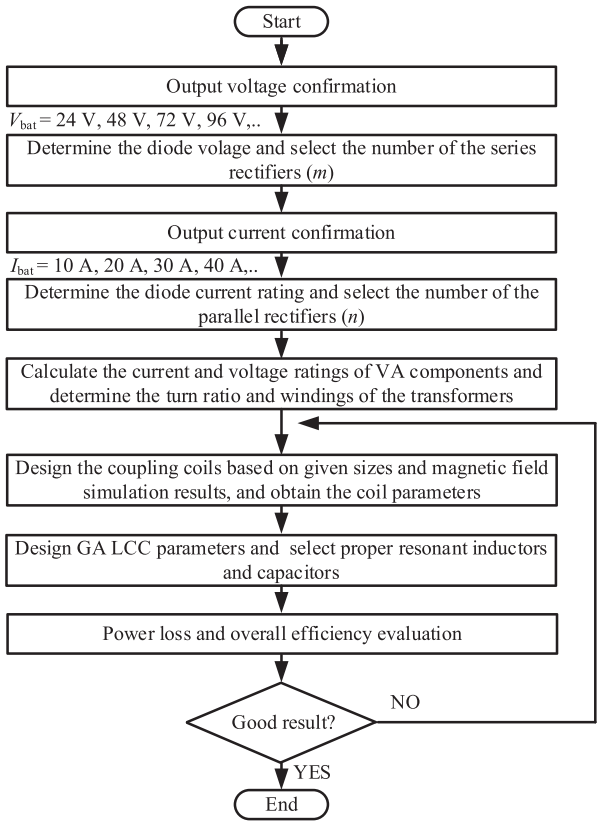

Fig. 10. Design procedure of the proposed WPT system.

(5)–(8). The resonant currents on the GA can be calculated as well. Then, inductors and capacitors with proper rated currents and voltages are selected.

The final step is to build up a prototype and evaluate the power losses and overall efficiency. One can repeat the above steps until the system performance is satisfied.

IV. Experimental Verification

An underwater WPT system is built to verify the proposed method, whose photograph is shown in Fig. 11. The key parameters are listed in Table I. The inverter is supplied by a programmable dc voltage source Chroma 62100H-600S. The experimental waveforms are recorded by an eight-channel wavescope platform ZLG ZDL6000. NVH4L020N090SC1 SiC MOSFETs and VBT3045CBP diodes are used for the inverter and the rectifiers, respectively. The inverter is controlled by a digital signal processor TMS320F28335. Two similar coils are used for the magnetic coupler. The coil dimensions of them are 37 cm × 48.5 cm ×2 cm. Litz wires are used to reduce the parasitic resistances. The self-inductances for the transmitting and receiving coils are around 153 μH and 149 μH, respectively. One can optimize the coil dimensions according to specific AUV size requirements. 64-L water and 2250-g salt are mixed in a tank, which means the salt concentration in seawater is around 3.5%. The coils are put inside the tank, whose power transfer medium between coils is seawater. The turns ratio of VA transformers is 32:2:2. Since the current sharing and voltage

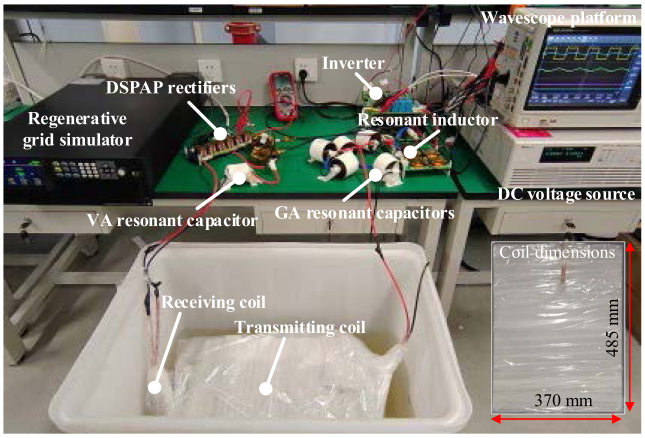

Fig. 11. Photograph of a multiple-voltage multiple-current underwater WPT system.

TABLE I
KEY PARAMETERS OF THE PROPOSED PROTOTYPE

Symbol	Parameter	Value
V_{bat}	Output voltage	48 V/72 V
I_{bat}	Output current	8 A–36 A
f	Operating frequency	85.5 kHz
$L_{f\ ga}$	Resonant inductor on the GA	45 μH
$C_{f\ ga}$	Filtering capacitor	78 nF
C_{ga}	Resonant capacitor	32 nF
L_{ga}	Self-inductance of Tx coil	153 μH
L_{va}	Self-inductance of Rx coil	149 μH
C_{va}	Resonant capacitor	23 nF
N_{va}	Turn ratios of VA transformers	32:2:2
R_{ga}	Parasitic resistance of Tx coil	0.5 Ω
R_{va}	Parasitic resistance of Rx coil	0.5 Ω
R_{s1}	Primary resistances of transformers	1.1 Ω
R_{s2}	Secondary resistances of transformers	8 mΩ
$R_{f\ ga}$	Parasitic resistance of $L_{f\ ga}$	40 mΩ
R_{dson}	Parasitic resistance of the MOSFET	10 mΩ
V_f	Forward voltage of the MOSFET	0.44 V

sharing characteristics are strongly related to their parameters, the self-inductances and leakage inductances of six transformers used in this prototype are measured. The magnetizing inductance and leakage inductance are around 1.6 mH and 3.7 μH, respectively. In addition, the leakage inductance tolerance is within 3%.

The rated voltage of the transformers is set at 24 V and the theoretical output voltage can be set at 24 V, where all the six rectifiers are connected in parallel. However, the output power is consumed by ITECH regenerative grid simulator IT7906P-350-90, whose minimum operating voltage is 30 V. Thus, this section demonstrates two groups of experiments based on the underwater WPT system including 48-V battery voltage, and 72-V battery voltage. To validate the performance of the proposed system against different charging currents, I_{bat} also changes from 25%, 50%, and 75% to 100%.

A. 48-V Battery Voltage With Different Charging Currents

Fig. 12 shows the schematic of the WPT system with 48-V battery voltage. The rated voltages of V_{bat1} and V_{bat2} are 24 V. Six rectifiers are divided into two groups: three rectifiers are

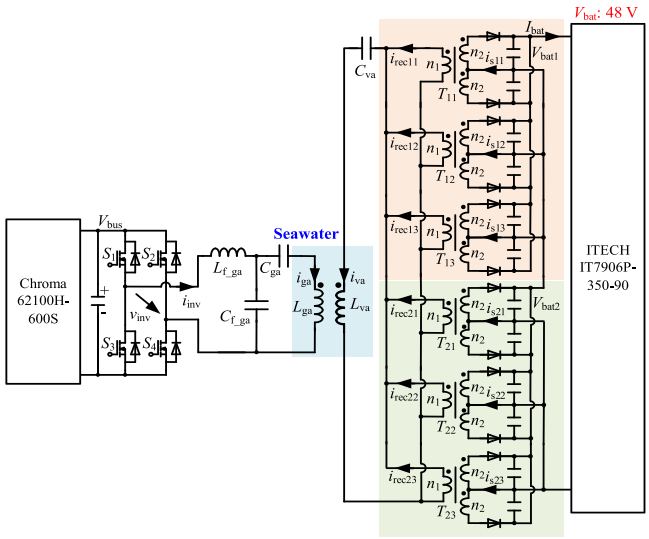

Fig. 12. Schematic of the WPT system with 48-V battery voltage, where $m = 2$ and $n = 3$.

TABLE II
EXPERIMENTAL RESULTS OF 48-V CHARGING

I_{bat}(A)	35.8	35.3	24.18	23.83	18.33	18.05	12.07	11.95
V_{bus}(V)	290	360	290	360	290	360	270	340
V_{bat}(V)	48.9	48.22	49.23	48.51	49.4	48.65	48.69	48.24
d(mm)	70	90	70	90	70	90	70	90
P_o(W)	1751	1702	1190	1156	906	878	588	576
η (%)	90.9	91.0	90.9	88.9	89.4	86.7	87.2	83.5

connected in parallel and two groups are connected in series. The power transfer distance d ranges from 70 mm to 90 mm, whose mutual inductances are 67 μH and 52 μH, respectively.

Fig. 13 shows the typical waveforms of the WPT system with 48-V battery voltage, including v_{inv}, i_{inv}, i_{va}, i_{rec11}, i_{rec13}, V_{bat1}, V_{bat2}, and I_{bat}. The experimental results are summarized in Table II. In Fig. 13(a), the output currents are 35.8 A and 35.3 A at 70 mm and 90 mm, respectively. The output powers are 1751 W and 1702 W, whose overall efficiencies are 90.9% and 91.0%, respectively. In Fig. 13(b), the output currents are 24.18 A and 23.83 A at 70 mm and 90 mm, respectively. The output powers are 1190 W and 1156 W with overall efficiencies of 90.9% and 88.9%, respectively. In Fig. 13(c), the output currents are 18.33 A and 18.05 A at 70 mm and 90 mm, respectively. The output powers are 906 W and 878 W and the overall efficiencies are 89.4% and 86.7%, respectively. In Fig. 13(d), the output currents are 12.07 A and 11.95 A at 70 mm and 90 mm, respectively. The output powers are 588 W and 576 W, corresponding to overall efficiencies of 87.2% and 83.5%, respectively.

The output power P_o ranges from 576 W to 1751 W and the dc–dc efficiency increases from 83.5% to 91.0%, which validates the power transfer analysis in Section II-B. Since the *LCC*-S has a constant voltage characteristic, V_{bus} changes little against different currents. As can be seen from the figures, the inverter operates with a 90° phase angle and ZVS operation is achieved. i_{rec11} and i_{rec13} are almost the same and V_{bat1} essentially overlaps V_{bat2}.

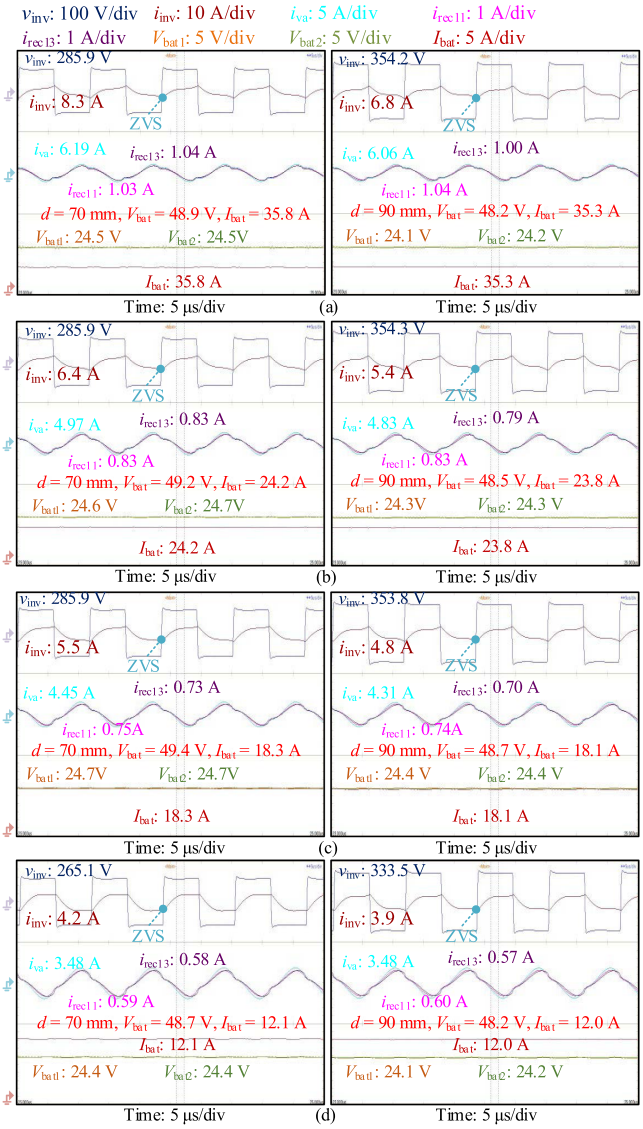

Fig. 13. Typical waveforms of the WPT system with 48-V battery voltage. (a) I_{bat} = 36 A. (b) I_{bat} = 24 A. (c) I_{bat} = 18 A. (d) I_{bat} = 12 A.

B. 72-V Battery Voltage With Different Charging Currents

Fig. 14 shows the schematic of the WPT system with 72-V battery voltage. The resonant components on the GA side and VA side remain the same. Six rectifiers are divided into three groups: two rectifiers are connected in parallel and three groups are connected in series. All the rated voltages of V_{bat1}-V_{bat3} are 24 V. The power transfer distance d and the mutual inductance remain the same as those in Section IV-A.

Fig. 15 shows the typical waveforms of the WPT system with 72-V battery voltage, including v_{inv}, i_{inv}, i_{rec11}, i_{rec21}, V_{bat1}, V_{bat2}, V_{bat3}, and I_{bat}. Table III summarizes the experimental results. In Fig. 15(a), the output currents are 23.77 A and 23.72 A at 70 mm and 90 mm, respectively. The output powers are 1711 W and 1705 W with overall efficiencies of 92.1% and 90.8%, respectively. In Fig. 15(b), the output currents are 16.01 A and 16.06 A at 70 mm and 90 mm, respectively. The output powers

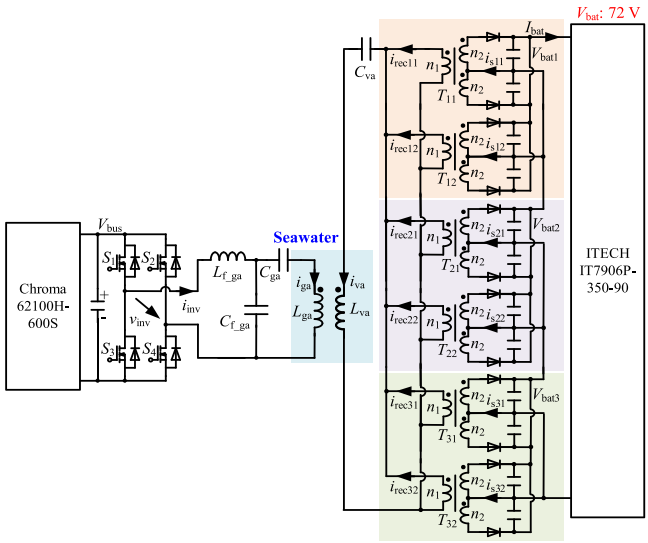

Fig. 14. Schematic of the WPT system with 72-V battery voltage, where m = 3 and n = 2.

TABLE III
EXPERIMENTAL RESULTS OF 72-V CHARGING

I_{bat}(A)	23.77	23.72	16.01	16.06	12.07	11.97	8.06	7.97
V_{bus}(V)	285	360	285	361	285	358	269	340
V_{bat}(V)	72.0	71.9	72.5	72.7	72.7	72.1	72.7	71.8
d(mm)	70	90	70	90	70	90	70	90
P_o(W)	1711	1705	1161	1168	878	863	586	572
η (%)	92.1	90.8	90.8	88.7	89.1	86.4	87.0	83.3

are 1161 W and 1168 W, whose overall efficiencies are 90.8% and 88.7%, respectively. In Fig. 15(c), the output currents are 12.07 A and 11.97 A at 70 mm and 90 mm, respectively. The output powers are 878 W and 863 W and the overall efficiencies are 89.1% and 86.4%, respectively. In Fig. 15(d), the output currents are 8.06 A and 7.97 A at 70 mm and 90 mm, respectively. The output powers are 586 W and 572 W, corresponding to overall efficiencies of 87.0% and 83.3%, respectively.

The output power P_o ranges from 572 W to 1711 W and the dc–dc efficiency increases from 83.3% to 92.1%, which validates the power transfer analysis in Section II-B. ZVS operation is also achieved by the inverter. V_{bat1}, V_{bat2}, and V_{bat3} overlap with each other, and i_{rec11} is almost equal to i_{rec21}.

Current sharing and voltage sharing are of great importance for the proposed DSPAP system. Therefore, different voltages and currents are measured in both 48-V and 72-V systems. To quantitatively evaluate them, voltage and current imbalance indexes are defined as Γ_V and Γ_I

$$\Gamma_V = \max\left(\frac{|V_{bat1}-V_{bat2}|}{V_{bat1}}, \frac{|V_{bat1}-V_{bat3}|}{V_{bat1}}\right) \tag{37}$$

$$\Gamma_I = \frac{|I_{rec11}-I_{rec13}|}{I_{rec11}} = \frac{|I_{rec11}-I_{rec21}|}{I_{rec11}}. \tag{38}$$

Fig. 16 shows the key performance indexes with respect to the output power P_o. *LCC*-S has a constant output voltage characteristic and a similar V_{bus} is required despite output current variations, which means I_{ga} changes little. In addition, a

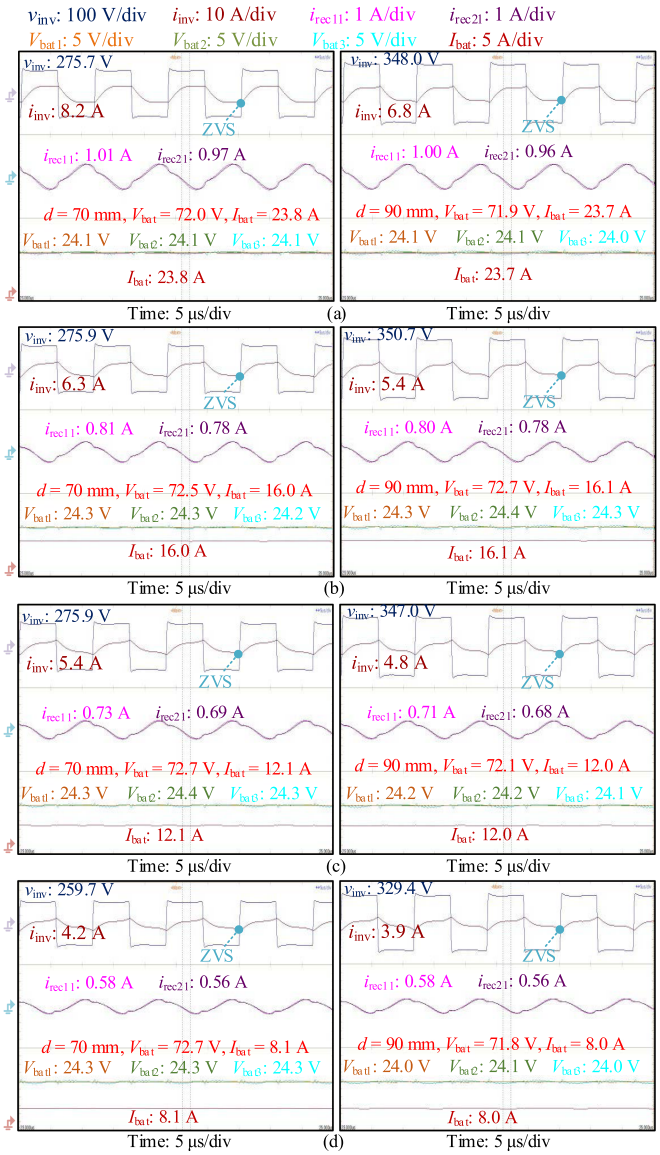

Fig. 15. Typical waveforms of the WPT system with 72-V battery voltage. (a) $I_{\mathrm{bat}} = 24$ A. (b) $I_{\mathrm{bat}} = 18$ A. (c) $I_{\mathrm{bat}} = 12$ A. (d) $I_{\mathrm{bat}} = 8$ A.

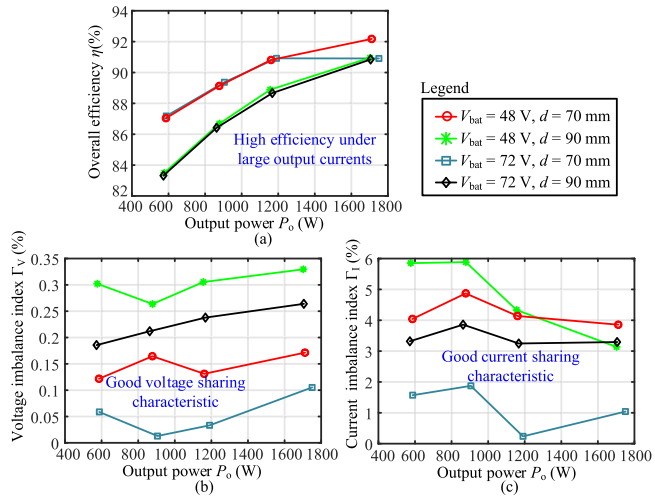

Fig. 16. Key performance indexes with respect to the output power P_{o}. (a) Overall efficiency η. (b) Voltage imbalance index Γ_{V}. (c) Current imbalance index Γ_{I}.

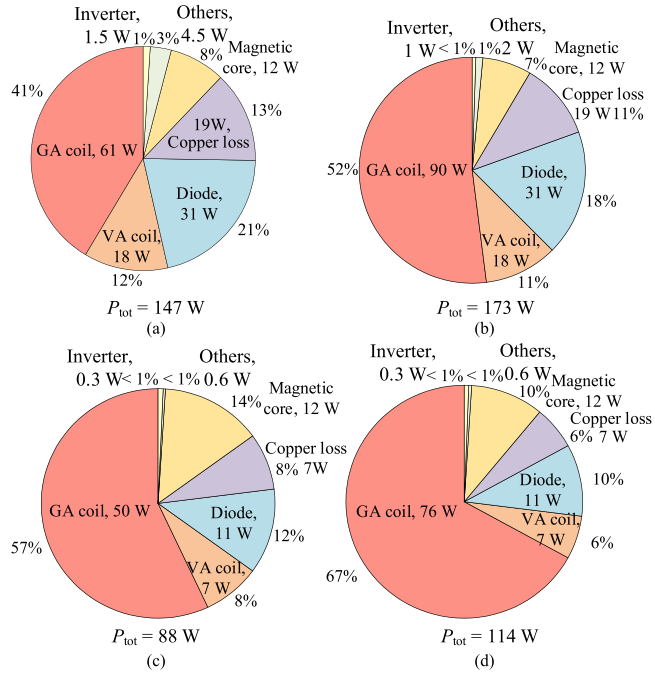

Fig. 17. Power loss breakdowns of the WPT system with 72-V battery voltage. (a) $P_{\mathrm{o}} = 1711$ W, $d = 70$ mm, $\eta = 92.1\%$. (b) $P_{\mathrm{o}} = 1705$ W, $d = 90$ mm, $\eta = 90.8\%$. (c) $P_{\mathrm{o}} = 586$ W, $d = 70$ mm, $\eta = 87.0\%$. (d) $P_{\mathrm{o}} = 572$ W, $d = 90$ mm, $\eta = 83.3\%$.

shorter power transfer distance corresponds to a higher mutual inductance, and smaller V_{bus} and I_{ga} are needed for the same V_{bat1}. Thus, transmitting coil loss as a percentage of input power decreases with increasing output power P_{o} and decreasing power transfer distance d. As shown in Fig. 16(a), the overall efficiency η increases with increasing output power and decreasing power transfer distance. A maximum overall efficiency of 92.1% is obtained. Fig. 16(b) and (c) shows the voltage and current imbalance indexes Γ_{V} and Γ_{I} with respect to different output power P_{o}. The maximum values of Γ_{V} and Γ_{I} are less than 0.35% and 6% under various conditions. Good voltage sharing and current sharing have been achieved, which validates the current sharing and voltage sharing analysis in Section III-B.

To demonstrate the power loss distribution intuitively, Fig. 17 shows the power loss breakdowns of the WPT system with 72-V battery voltage in four cases. In Fig. 17(a), the output power is 1711 W and the power transfer distance is 70 mm. The overall efficiency is 92.1% where the total power loss is 147 W. The loss generated by the GA coil is 61 W, which accounts for the largest share of 41% of the power loss. Because the output current is high, the forward voltage loss of the diodes is also large (31 W), corresponding to 21% of the share. In Fig. 17(b), the output power is 1705 W, and the power transfer distance is 90 mm. The system efficiency is 90.8% with a total power loss of 173 W. The GA coil produces the largest loss (90 W), which is 52% of the share. In Fig. 17(c), the output power is 586 W and the

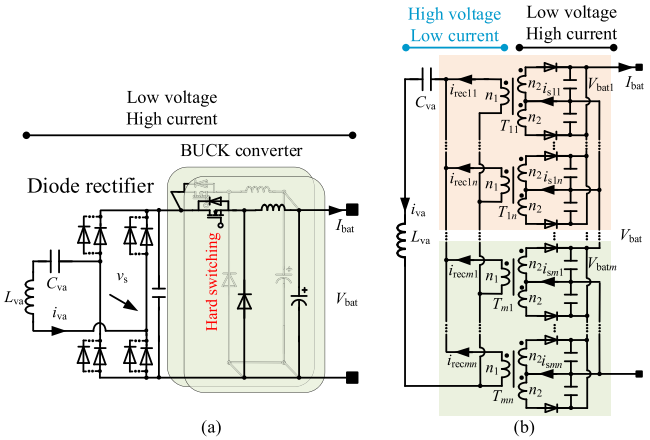

Fig. 18. Comparison of conventional and proposed receiver. (a) Conventional receiver with a BUCK converter. (b) Proposed receiver.

TABLE IV
COMPARISON BETWEEN DIFFERENT SYSTEMS

Ref.	V_{bat} (V)	I_{bat} (A)	η (%)
[11]	188–200	15–16	89–91.9
[12]	48.9–63.3 (*)	1.63–2.11	~60–82
[13]	100	3.21–7.45	76.2–86.2
[14]	8.3–21.2 (*)	1.1–2.9 (*)	58–73.8
[15]	/	/	~86–92.3
[16]	10–25	0.9–2.5	40–70.5
[17]	/	/	28–75
[18]	56.7 (*)	2.23	80
[19]	62.5 (*)	3.2 (*)	81.5–89.5
[20]	77.5 (*)	2.58 (*)	62–85
This paper	48/72	8-36	83.3–92.1

Note: * means that the data is estimated.

power transfer distance is 70 mm. The overall efficiency is 87.0% with a total power loss 88 W. The GA coil produces 57% of the total power loss, which is around 50 W. In Fig. 17(d), the output power is 572 W, the power transfer distance is 90 mm, the system efficiency is 83.3% whose total loss is 114 W. The GA coil produces 76-W power loss, i.e., 67% of the share. In summary, most of the power loss is generated by the GA coil, and the forward voltage loss is also large with a large output current. In addition, at the same output power, the larger the coupling coefficient, the smaller the loss and the higher the efficiency due to a smaller I_{ga}.

C. Comparison and Discussions

To show the contribution of this work more intuitively, as shown in Fig. 18, comparison and discussion between conventional and proposed receiver are presented here.

Table IV presents the charging voltages, currents, and overall efficiencies of different underwater WPT systems for AUVs. Generally, the output voltage is low due to the requirement of AUV battery packs. The overall efficiency is also low due to the eddy loss of the seawater. The rated voltage and rated current of these systems are fixed and few works discuss the realization of a high-current WPT system. Although only 48-V and 72-V voltages are conducted due to the limited of the test equipment,

TABLE V
COMPARISON BETWEEN DIFFERENT TOPOLOGIES

	Conventional topology in Fig. 1(b)	This paper
Current flexibility	No	Yes
Voltage flexibility	No	Yes
Forward diode voltage loss	Two	One
VA dc–dc converters	Alternative	No
Modular design	No	Yes
High output current	Not discussed	Yes
Natural current sharing	No	Yes
Secondary regulation	Yes	No
VA coil current	Higher	Lower
Overall efficiency	Lower	Higher
Volume and weight	Larger and heavier	Smaller and lighter
VA cost	Higher	Lower
Diodes	4*mn*	2*mn*
MOSFETs	*mn*	0
Driver circuits	*mn*	0
Inductors	*mn*	0
Filtering capacitors	2*mn*	*mn*
Transformers	0	*mn*
Current sampling circuits	*mn*	1
Voltage sampling circuits	2	1
Number of hard switching	*mn*	0

Note: the number of BUCK converters is supposed to be *mn*.

the proposed can adapt to various applications with different voltages and currents.

The differences between the conventional and the proposed systems are further summarized in Table IV. The differences between the BUCK converters and inverters of the two systems are summarized in Table V. More components including 2*mn* diodes, *mn* MOSFETs, *mn* driver circuits, *mn* BUCK inductors, *mn* filtering capacitors, and 1 voltage sampling and *mn*–1 current sampling circuits are used in the conventional receiver. In addition, it suffers from *mn* times of hard switching, which means the overall efficiency may be degraded significantly. Although *mn* transformers are used in the proposed receiver, their size and cost may be slightly lower than those of *mn* BUCK inductors due to the high resonant frequency. It can be seen that the proposed system takes the advantages of flexible and high output currents, flexible charging battery voltages, fewer diode forward voltage losses, compact receiver architecture, and modular design for higher power improvement. The high current only exists on the rectifier side, which can significantly reduce the power loss of the Rx coil. Natural current sharing and voltage sharing can be obtained by the proposed topology, which helps to power improvement. In summary, fewer components are used in the proposed topology and higher efficiency can be obtained, which contributes to a lower cost and a higher power density.

Admittedly, this proposed VA also has some shortcomings. A current inrush may occur if V_{bat} drops quickly. The output voltage cannot be regulated on the VA side due to the usage of diode rectification. Changing the series rectifier can only yield a finite number of voltage levels, such as multiple times of 24 V in this article. However, it should be noted that each rectifier can work normally within the range of [16 V, 32 V], which is a typical voltage range of a single battery pack. This contributes to the realization of a continuous output voltage. In the future work, the active rectifier or the frequency shift control can be applied to the inverter for output power regulation.

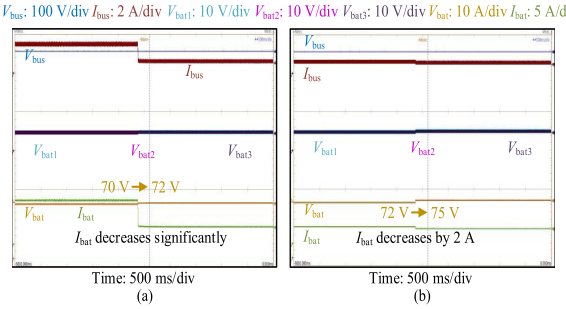

Fig. 19. Typical waveforms of the *LCC*-S WPT system when the battery voltage fluctuates. (a) 70 V–72 V. (b) 72 V–75 V.

V. Conclusion

The voltage ratings and current ratings of AUV WPT systems are increasing to increase working times. However, emerging specifications are making system design difficult and few works discuss the realization of the AUV WPT systems with multiple charging voltages and currents. This article proposes a DSPAP-based architecture, which can adapt to different battery voltages and charging currents without adding additional dc–dc circuits. It achieves natural current and voltage sharing and has the advantages of high design flexibility and modular hardware design, which benefits voltage compatibility and current improvement. The proposed system can be used for different specifications without significant parameter changes. A 1.7-kW AUV WPT platform with battery voltages of 48 V and 72 V has been built. The output current ranges from 8 A to 36 A with a maximum dc–dc efficiency of 92.1%, and the feasibility of the proposed architecture is proved.

Appendix

Fig. 19 presents the measured input and output voltages and currents with battery voltage fluctuations where three rectifiers are connected in series. The input voltage $V_{\rm bus}$, input current $I_{\rm bus}$, rectifier voltages ($V_{\rm bat1}$, $V_{\rm bat2}$, and $V_{\rm bat3}$), output voltage $V_{\rm bat}$, and output current $I_{\rm bat}$ are recorded. In Fig. 19(a), $I_{\rm bat}$ decreases by $\sim$10 A. In Fig. 19(b), $I_{\rm bat}$ decreases by around 2 A. In addition, a good dynamic voltage sharing has been achieved as three rectifier voltages overlap with each other. Without changing the input voltage or the operating frequency, the result of a battery voltage fluctuates is the decrease of output current, which will not result in any hardware faults. In practical applications, the battery voltage increases slowly. Thus, the output current can be regulated by control methods including regulating the input voltage $V_{\rm bus}$ and the switching frequency of the inverter.

References

[1] Z. Yan, B. Song, Y. Zhang, K. Zhang, Z. Mao, and Y. Hu, "A Rotation-Free wireless power transfer system with stable output power and efficiency for autonomous underwater vehicles," *IEEE Trans. Power Electron.*, vol. 34, no. 5, pp. 4005–4008, May 2019.

[2] Z. Yan et al., "Free-Rotation wireless power transfer system based on composite Anti-Misalignment method for AUVs," *IEEE Trans. Power Electron.*, vol. 38, no. 4, pp. 4262–4266, Apr. 2023.

[3] Z. Yan, K. Zhang, L. Qiao, Y. Hu, and B. Song, "A multiload wireless power transfer system with concentrated magnetic field for AUV cluster system," *IEEE Trans. Ind. Appl.*, vol. 58, no. 1, pp. 1307–1314, Jan./Feb. 2022.

[4] J. X. Wang, M. Zhong, Z. Wu, M. Guo, X. Liang, and B. Qi, "Ground-based investigation of a directional, flexible, and wireless concentrated solar energy transmission system," *Appl. Energy*, vol. 322, Sep. 2022, Art. no. 119517.

[5] Y. Chen et al., "A clamp Circuit-Based inductive power transfer system with reconfigurable rectifier tolerating extensive coupling variations," *IEEE Trans. Power Electron.*, vol. 39, no. 2, pp. 1942–1946, Feb. 2024.

[6] L. Yang, M. Ju, and B. Zhang, "Bidirectional undersea capacitive wireless power transfer system," *IEEE Access*, vol. 7, pp. 121046–121054, 2019.

[7] A. Khaligh and M. D'Antonio, "Global trends in High-Power On-Board chargers for electric vehicles," *IEEE Trans. Veh. Technol.*, vol. 68, no. 4, pp. 3306–3324, Apr. 2019.

[8] H. Li, K. Wang, J. Fang, and Y. Tang, "Pulse density modulated ZVS Full-Bridge converters for wireless power transfer systems," *IEEE Trans. Power Electron.*, vol. 34, no. 1, pp. 369–377, Jan. 2019.

[9] H. Li, J. Fang, S. Chen, K. Wang, and Y. Tang, "Pulse density modulation for maximum efficiency point tracking of wireless power transfer systems," *IEEE Trans. Power Electron.*, vol. 33, no. 6, pp. 5492–5501, Jun. 2018.

[10] Y. Chen, H. Zhang, C. S. Shin, C. H. Jo, S. J. Park, and D. H. Kim, "An efficiency optimization-based asymmetric tuning method of Double-Sided LCC compensated WPT system for electric vehicles," *IEEE Trans. Power Electron.*, vol. 35, no. 11, pp. 11475–11487, Nov. 2020.

[11] D. Wang, S. Cui, J. Zhang, Z. Bie, K. Song, and C. Zhu, "A novel Arc-Shaped lightweight magnetic coupler for AUV wireless power transfer," *IEEE Trans. Ind. Appl.*, vol. 58, no. 1, pp. 1315–1329, Jan./Feb. 2022.

[12] K. Zhang, X. Zhang, Z. Zhu, Z. Yan, B. Song, and C. C. Mi, "A new coil structure to reduce Eddy current loss of WPT systems for underwater vehicles," *IEEE Trans. Veh. Technol.*, vol. 68, no. 1, pp. 245–253, Jan. 2019.

[13] T. Kan, Y. Zhang, Z. Yan, P. P. Mercier, and C. C. Mi, "A Rotation-Resilient wireless charging system for lightweight autonomous underwater vehicles," *IEEE Trans. Veh. Technol.*, vol. 67, no. 8, pp. 6935–6942, Aug. 2018.

[14] S. Pang, J. Xu, H. Li, Q. Ma, and X. Li, "Dual-Frequency modulation to achieve power independent regulation for Dual-Load underwater wireless power connector," *IEEE J. Emerg. Sel. Topics Power Electron.*, vol. 11, no. 2, pp. 2377–2389, Apr. 2023.

[15] Y. Zeng, C. Lu, R. Liu, X. He, C. Rong, and M. Liu, "Wireless power and data transfer system using multidirectional magnetic coupler for swarm AUVs," *IEEE Trans. Power Electron.*, vol. 38, no. 2, pp. 1440–1444, Feb. 2023.

[16] J. Xu, X. Li, H. Li, Z. Xie, and Q. Ma, "Maximum efficiency tracking for Multi-Transmitter Multi-receiver wireless power transfer system on the submerged Buoy," *IEEE Trans. Ind. Electron.*, vol. 69, no. 2, pp. 1909–1919, Feb. 2022.

[17] C. Yang, T. Wang, and Y. Chen, "Design and analysis of an omnidirectional and positioning tolerant AUV charging platform," *IET Power Electron*, vol. 12, no. 8, pp. 2108–2117, Jul. 2019.

[18] K. Zhang, Y. Ma, Z. Yan, Z. Di, B. Song, and A. P. Hu, "Eddy current loss and detuning effect of seawater on wireless power transfer," *IEEE J. Emerg. Sel. Topics Power Electron.*, vol. 8, no. 1, pp. 909–917, Mar. 2020.

[19] Z. Yan et al., "Frequency optimization of a loosely coupled underwater wireless power transfer system considering Eddy current loss," *IEEE Trans. Ind. Electron.*, vol. 66, no. 5, pp. 3468–3476, May 2019.

[20] J. Kim, K. Kim, H. Kim, D. Kim, J. Park, and S. Ahn, "An efficient modeling for underwater wireless power transfer using *Z* -Parameters," *IEEE Trans. Electromagn. Compat.*, vol. 61, no. 6, pp. 2006–2014, Dec. 2019.

[21] G. Yang et al., "Improved interoperability evaluation method for wireless charging systems based on interface impedance," *IEEE Trans. Power Electron.*, vol. 36, no. 8, pp. 8588–8592, Aug. 2021.

[22] W. X. Zhong and S. Y. R. Hui, "Maximum energy efficiency tracking for wireless power transfer systems," *IEEE Trans. Power Electron.*, vol. 30, no. 7, pp. 4025–4034, Jul. 2015.

[23] X. Liu, T. Wang, F. Gao, M. M. Khan, X. Yang, and D. J. Rogers, "A resonant inductor Integrated-Transformer-based receiver for wireless power transfer systems," *IEEE Trans. Ind. Electron.*, vol. 70, no. 4, pp. 3616–3626, Apr. 2023.

[24] X. Liu, F. Gao, H. Niu, G. Sun, T. Wang, and H. Wang, "A Series-Parallel Transformer-Based WPT system for 400-V and 800-V electric vehicles with Z1 or Z2 class," *IEEE Trans. Power Electron.*, vol. 39, no. 1, pp. 1749–1761, Jan. 2024.

[25] E. Serban, C. Pondiche, and M. Ordonez, "Analysis and design of bidirectional Parallel-Series DAB-Based converter," *IEEE Trans. Power Electron.*, vol. 38, no. 8, pp. 10370–10382, Aug. 2023.

[26] "Wireless power transfer for Light-Duty Plug-In/Electric vehicles and alignment methodology," International Standard SAE J2954, 2019. [Online]. Available: https://www.sae.org/standards/content/j2954_201904/
[27] N. Fu, J. Deng, Z. Wang, W. Wang, and S. Wang, "A hybrid mode control strategy for LCC–LCC-Compensated WPT system with wide ZVS operation," *IEEE Trans. Power Electron.*, vol. 37, no. 2, pp. 2449–2460, Feb. 2022.
[28] Z. Cheng, Y. Lei, K. Song, and C. Zhu, "Design and loss analysis of loosely coupled transformer for an underwater High-Power inductive power transfer system," *IEEE Trans. Magn.*, vol. 51, no. 7, Jul. 2015, Art. no. 8401110.

Xin Liu (Member, IEEE) received the B.S. degree from Wuhan University, Wuhan, China, in 2015, and the Ph.D. degree from Shanghai Jiao Tong University, Shanghai, China, in 2019, both in electrical engineering.

From 2019 to 2021, he was with Huawei Technologies Co., Ltd. From 2021 to 2023, he was with the Department of Electrical Engineering, Shanghai Jiao Tong University, Shanghai, China, as a Postdoctoral Researcher. Since 2023, he has been with the Shenzhen Institute for Advanced Study, University of Electronic Science and Technology of China, Chengdu, China, as an Associate Researcher. His current research interests include wireless power transfer and solid state transformers.

Ruizhi Chen received the B.S. degree in electronic science and technology from Chongqing University of Posts and Telecommunications, Chongqing, China, in 2021. He is currently working toward the M.S. degree in control science and engineering with the Shenzhen Institute for Advanced Study, University of Electronic Science and Technology of China, Shenzhen, China.

His research interest includes wireless power transfer in seawater.

Fangli Li received the B.S. degree in computer science and technology from Beijing Electronic Science and Technology Institute, Beijing, China, in 2008, and the master's degree in public management from Shenzhen University, Shenzhen, China, in 2014.

Since 2011, he has been with Shenzhen Development and Reform Commission, successively held positions with the high technology department, major projects department, and innovation ability department. He has mainly responsible for the related work of Guangming Science City, participate in the planning of major science and technology infrastructure in Guangming Science City. His current research interests include system architecture and engineering management.

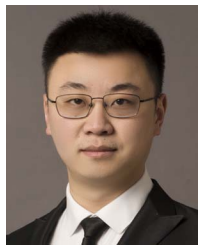

Dehong Zhou (Senior Member, IEEE) received the B.Sc. and Ph.D. degrees in control science and engineering from Huazhong University of Science and Technology, Wuhan, China, in 2012 and 2016, respectively.

From 2016 to 2018, he was a Postdoctoral Research Fellow with Nanyang Technological University, Singapore. From 2018 to 2020, he was a Postdoctoral Fellow with University of Alberta, Canada. Since 2020, he has been a Full Professor with the School of Automation Engineering, University of Electronic Science and Technology of China (UESTC), Chengdu, China, and with the Shenzhen Institute for Advanced Study, UESTC, Shenzhen, China. His research interests include power electronics and motor drives.

Jianxiao Zou (Member, IEEE) received the B.S., M.S., and Ph.D. degrees in control science and engineering from the University of Electronic Science and Technology of China (UESTC), Chengdu, China, in 2000, 2003, and 2009, respectively.

He is currently a Professor with UESTC, and has been the Vice Dean with Shenzhen Institute for Advanced Study, UESTC, since 2020. He was a Visiting Scholar with the University of California, Berkeley, CA, USA, in 2010, and a Senior Visiting Professor with Rutgers, the State University of New Jersey, New Brunswick, NJ, USA, in 2014. His current research interests include control theory and control engineering, renewable energy control technologies, and intelligent information processing and control.